OUTSTANDING SYMPOSIUM PAPER

Articles in this section are based on presentations that were selected by MRS Meeting Symposium Organizers as outstanding papers. Upon selection, authors are invited to submit their research results to Journal of Materials Research. *These papers are subject to the same peer review and editorial standards as all other JMR papers. This is another way by which the Materials Research Society recognizes high quality papers presented at its meetings.*

3D x-ray microprobe investigation of local dislocation densities and elastic strain gradients in a NiAl-Mo composite and exposed Mo micropillars as a function of prestrain

Rozaliya I. Barabash[a)]
Materials Science and Technology Division, Oak Ridge National Laboratory, Oak Ridge, Tennessee 37831; and Materials Science and Engineering Department, University of Tennessee, Knoxville, Tennessee 37996

Hongbin Bei[b)]
Materials Science and Technology Division, Oak Ridge National Laboratory, Oak Ridge, Tennessee 37831

Yanfei Gao
Materials Science and Engineering Department, University of Tennessee, Knoxville, Tennessee 37996; and Computer Science and Mathematics Division, Oak Ridge National Laboratory, Oak Ridge, Tennessee 37831

Gene E. Ice
Materials Science and Technology Division, Oak Ridge National Laboratory, Oak Ridge, Tennessee 37831

Easo P. George
Materials Science and Technology Division, Oak Ridge National Laboratory, Oak Ridge, Tennessee 37831; and Materials Science and Engineering Department, University of Tennessee, Knoxville, Tennessee 37996

(Received 12 August 2009; accepted 6 November 2009)

3D spatially-resolved polychromatic microdiffraction was used to nondestructively obtain depth-dependent elastic strain gradients and dislocation densities in the constituent phases of a directionally solidified NiAl–Mo eutectic composite consisting of ~500–800 nm Mo fibers in a NiAl matrix. Measurements were made before and after the composite was compressed by 5% and 11%. The Mo fibers were analyzed both in their embedded state and after the matrix was etched to expose them as pillars. In the as-grown composite, due to differential thermal contraction during cooldown, the Mo phase is under compression and the NiAl phase is in tension. After the prestrains, the situation is reversed with the Mo phase in tension and NiAl matrix in compression. This result can be explained by taking into account the mismatch in yield strains of the constituent phases and the elastic constraints during unloading. The dislocation density in both the Mo and NiAl phases is found to increase after prestraining. Within experimental uncertainty there is little discernible difference in the total dislocation densities in the Mo phase of the 5% and 11% prestrained specimens. However, the density of the geometrically necessary dislocations and the deviatoric strain gradients increase with increasing prestrain in both the Mo and NiAl phases.

I. INTRODUCTION

Micropillar compression testing has become a popular way to characterize the mechanical behavior of small volumes of materials, following the seminal work of Uchic et al.[1] Typically, the pillars are fabricated by focused ion beam (FIB) milling and pillar diameters ranging from hundreds of nanometers to tens of micrometers have been tested. Interesting size effects ("smaller is stronger") have

Address all correspondence to these authors:
[a)]e-mail: Barabashr@ornl.gov
[b)]e-mail: Beih@ornl.gov
This paper was selected as an Outstanding Symposium Paper for the 2008 MRS Fall Meeting, Symposium EE Proceedings, Vol. 1137E. To maintain *JMR*'s rigorous, unbiased peer review standards, the *JMR* Principal Editor and reviewers were not made aware of the paper's designation as Outstanding Symposium Paper.
DOI: 10.1557/JMR.2010.0043

 © 2010 Materials Research Society

been identified below sizes of ~10–20 μm.[2–7] An alternative technique of micropillar testing involves directional solidification (DS) of fibrous eutectics, for example, NiAl-Mo,[8] followed by etching of the matrix to expose the fibers as pillars for compression.[9,10] Molybdenum alloy pillars produced by the DS route show some significant differences relative to their FIB counterparts. For example, the directionally solidified pillars behave like dislocation-free whiskers and yield at close to the theoretical strength independent of size over a fairly wide size range of pillar sizes, ~360–1400 nm[9–11] unlike FIB-milled Mo pillars which yield at significantly lower stresses.[12] Interestingly, when the directionally solidified NiAl-Mo composite was prestrained before the matrix was etched, the yield strengths of the exposed Mo pillars were found to be dramatically lower than those of the as-grown pillars.[10] Additionally, their subsequent stress-strain behavior was found to be closely related to the amount of prestrain, with stochastic, stair-step-shaped flow curves at ~4–8% prestrain, and relatively smooth, reproducible, bulk-like flow curves with stable work hardening at 11% prestrain.[10] In general, the scatter in the stress-strain curves decreases with increasing pillar size for a given prestrain, and with increasing prestrain for a given pillar size.[10] FIB milling of the DS pillars dramatically lowered their strengths,[13] consistent with what others have generally reported for FIB-milled pillars, namely, that they yield at stresses much below the theoretical strength.[9]

To understand the small-scale mechanical behavior of micropillars, it is critical to develop techniques to characterize their defect distributions at appropriate length scales. Transmission electron microscopy has been used to analyze the defects present in FIB-milled pillars[7] but, since the FIB process can introduce a variety of defects,[14–16] it is not straightforward to separate their effects from those of the deformation-induced defects. Nor is it easy to unambiguously determine how the FIB damage evolves during subsequent microcompression. For example, as the pillar size decreases, both decreases[7] and increases[17] in dislocation density have been reported after compression. It would be useful, therefore, to analyze pillars produced without FIB milling and characterize the changes in their dislocation distributions after deformation, which is our objective in this paper.

Recently, x-ray beams have become available with beam sizes down to ~100 nm. These small penetrating beams can be used to probe very small volumes of materials to determine local strain gradients and defect states.[18–21] We show here how microfocused x-ray beams can be used to characterize the behavior of the DS NiAl-Mo composite given different amounts of prestrain. Previously we have shown that, in the as-grown state, the mismatch in thermal expansion coefficients between NiAl and Mo phases[22] creates elastic strains in both the matrix and fibers.[20] The elastic strain in the fibers is relaxed when the matrix is etched away, leaving the exposed Mo pillars essentially strain free.[20] In this study, we focus on the responses of the NiAl and Mo phases to externally applied uniaxial compression (prestrain), and estimate from x-ray line-broadening the total dislocation densities in the pillars before and after prestraining. The technique described here is applicable to composite materials in general, where information about phase-specific strains is useful in understanding the mechanical response.

II. EXPERIMENTAL

A. Specimen preparation

The directionally solidified NiAl-Mo eutectic investigated in this study has a relatively simple microstructure, consisting of long Mo fibers embedded in an NiAl matrix.[8,23] The fiber size and spacing vary inversely as the square root of the growth rate. Details of the directional solidification process and the resulting composite microstructures have been described previously.[8] Figure 1(a)

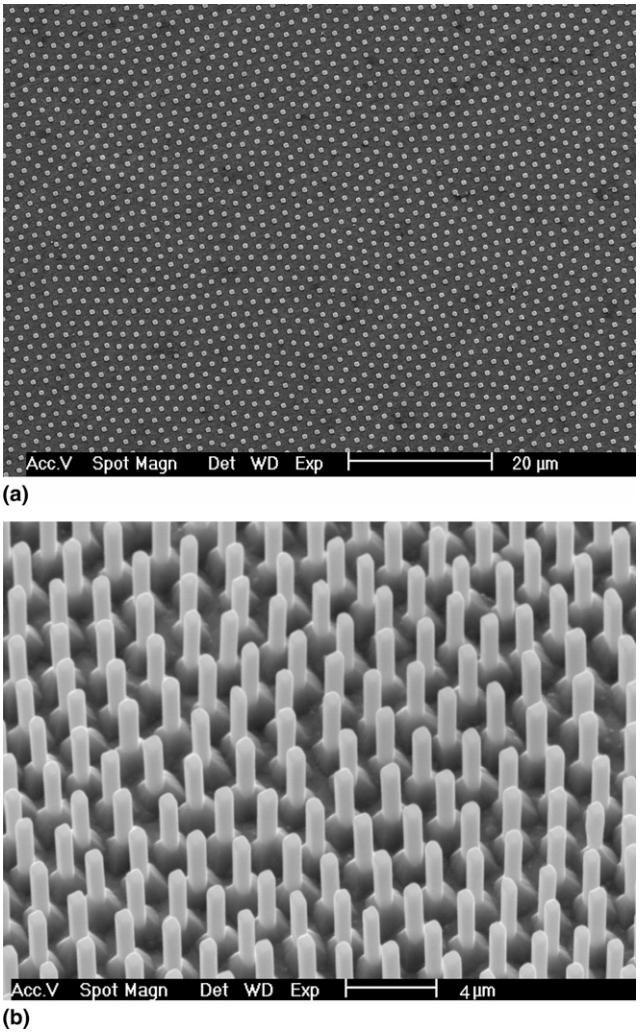

FIG. 1. SEM images of the as-grown NiAl-Mo eutectic: (a) before the NiAl matrix is etched and (b) after etching to reveal exposed pillars.

shows a plan view of the composite, with fiber sizes (edge lengths of the approximately square cross-section fibers) ranging from ~500–800 nm. Figure 1(b) shows the exposed fibers (pillars) after the NiAl matrix is etched away.

Disk-shaped specimens, ~2 mm thick, were cut from the directionally solidified NiAl-Mo eutectic perpendicular to the growth (fiber) direction. After grinding with SiC paper through 1200 grit, the disks were compressed in a hydraulic press with tungsten carbide platens. The amount of prestrain is defined here as the percentage reduction in thickness of the disks. Specimens subjected to two different prestrains, ~5%, and 11%, were investigated, in addition to the as-grown specimen (0% strain). All the specimens were mounted in epoxy, and ground and polished using standard metallographic procedures, first with SiC papers through 600 grit, and then with Al_2O_3 slurries through 0.3 μm. Finally, the specimens were polished with a colloidal silica suspension in a vibratory polishing machine. After polishing, some of the fibers were exposed by etching the NiAl matrix in a water solution containing 18% HCl and 8% H_2O_2. The exposed Mo pillars extended a few micrometers (~3–4 μm) beyond the surface of the NiAl matrix.

B. Polychromatic x-ray microdiffraction and differential aperture x-ray microscopy

The Mo fibers and NiAl matrix of the compressed samples were probed with polychromatic x-ray microdiffraction to obtain depth-dependent local elastic strains and total dislocation densities. Measurements were performed on station 34-ID-E at the Advanced Photon Source. Both etched and unetched specimens, containing embedded Mo fibers and exposed Mo pillars, respectively, were investigated by the x-ray microbeams. Depth-dependent elastic strains and dislocation densities were obtained using spatially resolved differential aperture x-ray microscopy (DAXM).[21,24–26]

For spatially-resolved measurements, a platinum wire was used as a knife edge. At each location, this aperture blocks the x-ray intensity scattered from different depths [Fig. 2(a)]. Displacement of this knife edge relative to the specimen surface creates a differential aperture, since the difference between images taken with the wire moved by small steps is due to x-rays passing near the upstream or downstream edge of the wire. Typically 400 partially shadowed images are used to triangulate the Laue intensity diffracted from different depths along the incident beam. Details of DAXM data collection can be found elsewhere.[21,24–26]

The Cartesian reference frame for the specimens is set such that the x and y axes are perpendicular to the pillars in the plane of the sample, and the z axis coincides with the growth direction, which is parallel to the [001] direction for both the Mo fibers and the NiAl matrix [Fig. 2(a)]. In this coordinate system, a polychromatic x-ray microbeam with a diameter less then 0.5 μm is incident on the surface at ~45° with incident components $\left(0, -1/\sqrt{2}, -1/\sqrt{2}\right)$. In this diffraction geometry, the beam probes regions located at different depths under the surface as it penetrates the sample. Both monochromatic and white beams were used in the present study. With polychromatic Laue measurements, parallel planes diffract in the same direction. For this reason (002), (004), (006) and other (00h)-type reflections are superimposed. To study changes in the lattice parameters, measurements with monochromatic beam were performed. The (006) reflection was chosen for both the Mo pillars and the matrix to obtain the inverse lattice parameter, Q, with modulus $|Q| = \frac{2\pi}{d}$, where d is the lattice spacing. The depth-resolved (006) d-spacing distribution was measured with an energy-scan method. The energy was scanned in 2-eV steps over a range of ~1000 eV through the (006) reflections of NiAl and Mo. Depth-dependent dislocation densities and elastic strain gradients were calculated from these measurements.

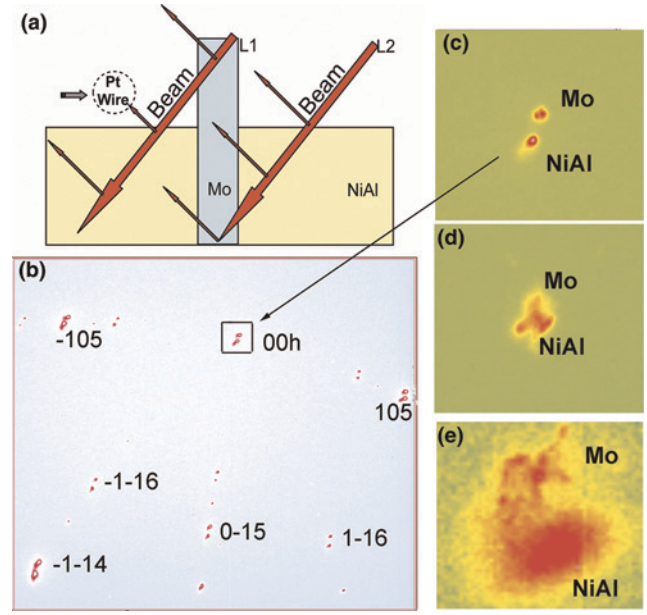

FIG. 2. (a) Sketch of the experimental geometry showing the interaction of the incident x-ray beam with the NiAl-Mo specimen and shadowing the diffracted x-rays by moving the Pt wire; (b) typical Laue pattern from the as-grown NiAl-Mo eutectic with two sets of Laue spots from NiAl and Mo; (c) enlarged regions around the (00h)-type reflections from NiAl and Mo in the as-grown eutectic, (d) enlarged regions around the (00h)-type reflections from NiAl and Mo in the 5% prestrained specimen, and (e) enlarged regions around the (00h)-type reflections from NiAl and Mo in the 11% prestrained specimen. Note that (c), (d), and (e) all have the same scale/resolution. (color online)

III. RESULTS AND DISCUSSION

In the as-grown eutectic composite, Mo fibers with sizes of ~500–800 nm are periodically located in the

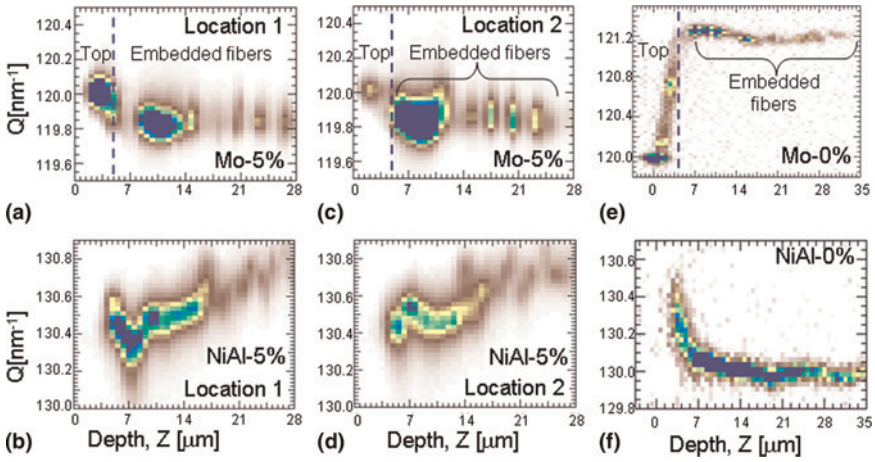

FIG. 3. Depth-dependent inverse lattice parameter, Q, for the NiAl and Mo phases of the eutectic composite from two different positions, corresponding to locations L1 and L2 shown in Fig. 2(a): (a) Mo and (b) NiAl both from L1 in the 5% prestrained specimen; (c) Mo and (d) NiAl both from L2 in the 5% prestrained specimen. Data in (e) and (f) are for the Mo and NiAl phases in the as-grown eutectic (0% prestrain). (color online)

NiAl matrix [Fig. 1(a)]. A typical Laue pattern of the as grown NiAl-Mo composite is shown in Fig. 2(b). The slight misorientation (~0.3°) between the NiAl matrix and Mo fibers is the reason that all the Laue spots in the pattern consist of two separate peaks, one belonging to the matrix and the other to the Mo fibers [Figs. 2(b) and 2(c)]. This indicates that the Mo (001) and NiAl (001) planes are not exactly parallel to each other. On the other hand, such small tilts (~0.3°) are evidence of the very good crystallographic quality of the as-grown composite. An enlarged region of interest around the (00h)-type Laue spot [Fig. 2(c)] is found to contain separate Laue spots for NiAl and Mo. In each Laue spot, the upper peak is formed by diffraction from the Mo fibers and the bottom peak by diffraction from the NiAl matrix. For the as-grown (0% prestrained) specimen, all Laue spots are sharp, without any streaking, which is characteristic of a nearly perfect crystalline material with low defect concentrations.

Similar regions of the Laue pattern around the (00h)-type reflection after 5% and 11% prestrain are shown in Figs. 2(d) and 2(e) [at the same scale/resolution as in Fig. 2(c)]. The subpeaks belonging to both the NiAl matrix and the Mo fibers are significantly broader, indicating the formation of large strain gradients and/or geometrically necessary dislocation densities.

The results of depth resolved measurements of the inverse lattice parameter, Q, for the NiAl and Mo phases after 5% and 11% prestrain are shown in Figs. 3 and 4. In this two-phase NiAl-Mo composite, the tiny beam passes through volumes containing either only matrix or only pillars/fibers, depending on depth. As a result, the locations of maximum diffracted intensity from the Mo pillars correspond to locations of minimum diffracted intensity from the NiAl matrix and vice versa [compare

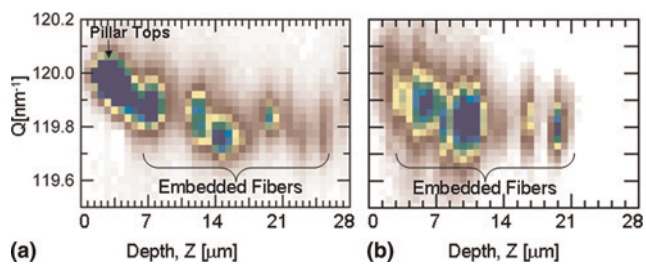

FIG. 4. Depth-dependent inverse lattice parameter, Q, for the Mo phase in the 11% prestrained specimen: (a) matrix etched to reveal exposed pillars; (b) unetched specimen with embedded fibers. (color online)

Figs. 3(a)–3(d)]. In the case of exposed Mo pillars with a height of 3–4 μm, the intensity from the tops of the Mo pillars is observed above the first depth at which matrix diffraction is observed [Figs. 3(a) and 3(b)]. For comparison, variations of Q with depth for the two phases of the undeformed eutectic composite (0% prestrain) are shown in Figs. 3(e) and 3(f). Using these results for the undeformed specimen as a reference, it is seen that the strain gradient distribution in both phases is reversed after compression. After 11% prestrain, the measured values of Q for the Mo pillars are similar to those after 5% prestrain (compare Figs. 3 and 4). In the as-grown (0% prestrained) composite [Figs. 3(e) and 3(f)], the embedded Mo fibers are under compression and the matrix is under tension along the [001] growth direction. In contrast, after the composite is prestrained by 5%, the Mo fibers are under ~0.16% tension [Figs. 3(a) and 3(c)] and the NiAl matrix is under compression [Figs. 3(b) and 3(d)]. Gaussian fits to the measured intensity profiles from the tops of the Mo pillars and from embedded fibers are shown in Fig. 5(a). The tops of the exposed pillars are practically strain-free both in the as-grown and

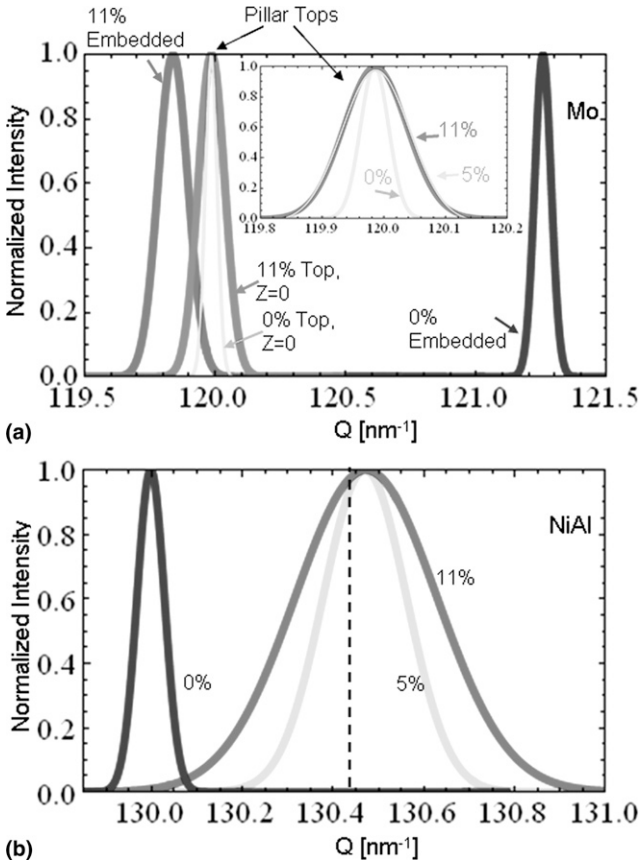

FIG. 5. (a) Intensity distributions from the tops of exposed pillars and embedded fibers in the 0% and 11% prestrained specimens showing strain reversal after prestraining; inset shows that pillar tops have the same lattice parameter regardless of prestrain but increased FWHM after prestraining; (b) Intensity distributions from the NiAl matrix at 10 μm under the surface demonstrate reversed strain in the matrix after prestraining. Dashed line shows Q value for strain-free NiAl matrix before deformation.

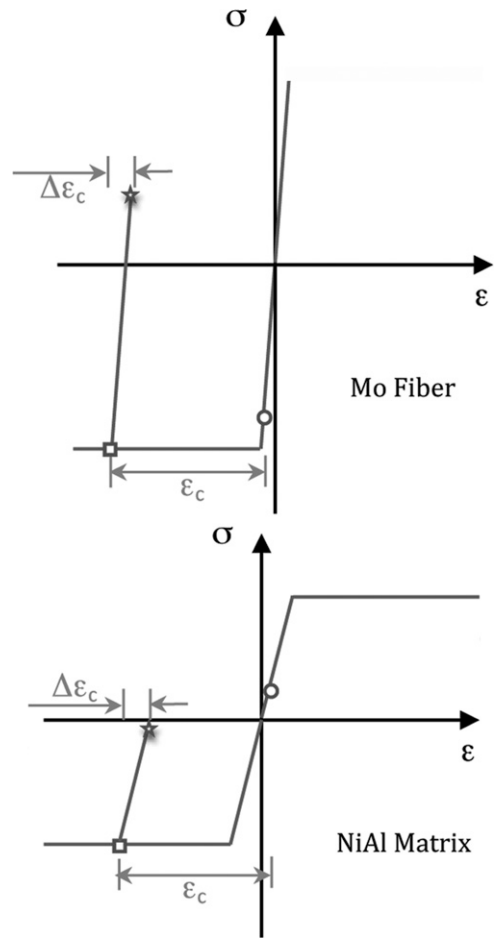

FIG. 6. Schematic diagram showing the residual strain and stress states in the Mo fibers and NiAl matrix. Circles: as-solidified state before compressive prestrain is applied; squares: under prestrain of ε_c; star: after elastic unloading of strain $\Delta\varepsilon_c$.

prestrained samples and have nearly the same lattice parameter [see the inset in Fig. 5(a)].

The measured residual strains in the Mo fibers and NiAl matrix before, during, and after prestrain can be understood by a simple stress analysis as illustrated in Fig. 6.

(i) As-grown stresses: As denoted by the circles along the stress/strain curve, the residual stress in the fibers along the [001] growth direction is compressive in the as-grown condition, whereas the stress in the matrix is tensile. These stresses arise naturally during the cool-down following solidification due to the smaller coefficient of thermal expansion of Mo compared to NiAl.[20,22] At temperatures down to ~600 °C, thermal expansion mismatch between the fibers and matrix is accommodated almost exclusively by plastic deformation of the NiAl matrix.[22] Below this temperature, the thermal mismatch generates compressive elastic strain in the Mo and tensile elastic strain in the NiAl.

(ii) Stresses after compression: When the composite is subjected to a uniaxial compressive strain, ε_c, the elastic stress has an increasingly negative component added to the original as-grown stress state until the yield stress is reached for both the matrix and fibers (Fig. 6). Beyond this point, additional strain is accommodated by plastic deformation of both the fiber and the matrix and the fully compressed sample stresses are indicated by the squares along the stress/strain curves of Fig. 6. Assuming that compression preserves the matrix/fiber continuity at the surfaces of the sample, the strain change is the same for the fibers and for the matrix; $\varepsilon_c^{\text{matrix}} = \varepsilon_c^{\text{fiber}} = \varepsilon_c$.

(iii) Stresses after unloading: When the composite is unloaded after compression, it expands elastically by $\Delta\varepsilon_c$ where again continuity requires that $\Delta\varepsilon_c^{\text{matrix}} = \Delta\varepsilon_c^{\text{fiber}} = \Delta\varepsilon_c$. Stress/strain states of the fiber and matrix after unloading are illustrated by the stars in Fig. 6. The stress in the matrix after unloading, σ_m, can be expressed in terms of the yield stress σ_Y^{matrix}, and the strain relaxation of the composite, $\Delta\varepsilon_c$; $\sigma_m = \sigma_Y^{\text{matrix}} + \Delta\varepsilon_c E_m$, where E_m

is the elastic modulus of the matrix. The stress in the fiber is given by a similar expression; $\sigma_f = \sigma_Y^{fiber} + \Delta\varepsilon_c E_f$ where E_f is the fiber elastic modulus. Substituting yield strains for yield stresses $\varepsilon_Y^{fiber} = \frac{\sigma_Y^{fiber}}{E_F}$, $\varepsilon_Y^{matrix} = \frac{\sigma_Y^{matrix}}{E_M}$, and equating the unloading strain of the fiber to the unloading strain of the matrix, we can eliminate $\Delta\varepsilon_c$ and obtain $\frac{\sigma_m}{E_m} - \frac{\sigma_f}{E_f} = \varepsilon_Y^{matrix} - \varepsilon_Y^{fiber}$. Additionally, with the force balance condition, $\sigma_m = -\sigma_f\left(\frac{V_f}{1-V_f}\right)$, we find, that

$$\frac{\sigma_f}{E_f}\left[1 + \frac{E_f}{E_M}\left(\frac{V_f}{1-V_f}\right)\right] = \varepsilon_Y^{fiber} - \varepsilon_Y^{matrix} \quad . \qquad (1)$$

If $\varepsilon_Y^{matrix} > \varepsilon_Y^{fiber}$, the residual stress state will be tension in the fibers and compression in the matrix. This would appear to be the case given that the NiAl and Mo phases have similar yield strengths (~1.0–1.2 GPa),[10,27] but the modulus of the Mo fibers is higher than that of the NiAl matrix.[8] The residual strain in the prestrained Mo fibers is measured to be ~0.16% (Figs. 3 and 4), which gives a value of σ_f = 0.43 GPa. Based on the above analysis and assuming a fiber modulus of 270 GPa and matrix modulus of 180 GPa,[8] the yield strain difference can then be calculated as $\varepsilon_Y^{matrix} - \varepsilon_Y^{fiber}$ = 0.23%. Therefore, the residual strain in the NiAl matrix after prestraining is predicted to be about –0.07%. Consistent with this analysis, the experimentally observed change of its inverse lattice constant, Q, is indeed small (~0.068%), as shown in Figs. 3(b), 3(d), and 5(b). Note that in our elastic-perfectly plastic model, the final residual stress state is determined solely by the yield/flow strengths of the two phases. Therefore, different values for the externally applied compressive strain, for example, ε_c = 5% or 11%, will not change the final residual stress state.

The intensity profiles corresponding to the tops of the as-grown pillars (0% prestrain) have a small full width at half maximum (FWHM) indicating a narrow range of strain variations and small dislocation densities. In contrast, the FWHM of reflections from the deformed Mo pillars are twice as broad [Fig. 5(b)], suggesting storage of dislocations in the prestrained pillars. The FWHM of reflections from the embedded Mo fibers also double after deformation [Fig. 5(a)]. Following the procedure discussed elsewhere,[24–26] the total dislocation density at different depths in the exposed pillars and embedded fibers was estimated after 5% and 11% prestrain (Fig. 7), and found to be ~10^9 cm^{-2}. However, within experimental uncertainty, no significant differences in dislocation density between the 5% and 11% prestrained specimens with comparable initial pillar sizes can be discerned in Fig. 7(b). In contrast, the dislocation density in the NiAl matrix increases with prestraining, from (2–4) × 10^9 cm^{-2} in the 5% prestrained specimen to 8 × 10^9 cm^{-2} in the 11% prestrained specimen [Fig. 7(c)]. An increase of dislocation density in the matrix was also observed by Misra et al.[23] after deformation of NiAl-Mo eutectic composites. Despite the above increase in dislocation density after prestraining, it is worth noting that the mean spacing between dislocations in the 500–800 nm micropillars studied here is still only about 300 nm, indicating that dislocation

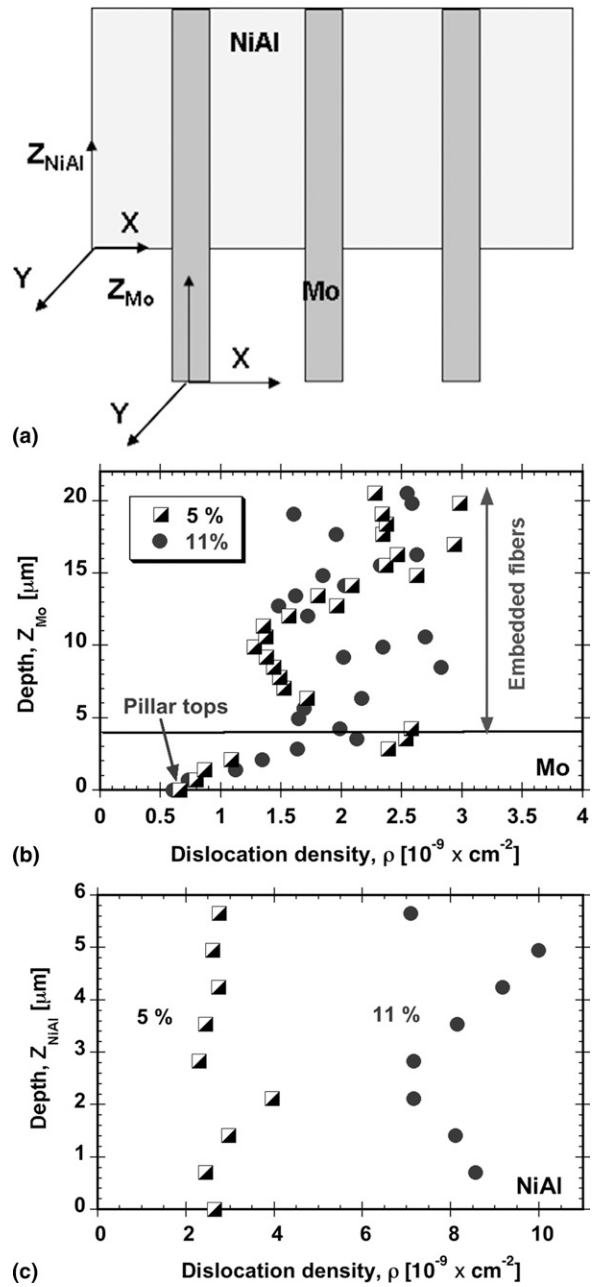

FIG. 7. (a) Sketch of the NiAl-Mo composite with coordinate systems indicating the Z = 0 planes for Mo pillars and NiAl matrix. (b) Calculated depth-dependent dislocation density distributions in the Mo phase after 5% (open square) and 11% (filled triangle) prestrain. The vertical dashed line separates the exposed pillars (on the bottom) from the embedded fibers (on the top). (c) Calculated depth-dependent dislocation density distributions in the NiAl matrix after 5% (square) and 11% (circle) prestrain.

multiplication appears to be required to accommodate subsequent pillar deformation. These results indicate that the dramatic differences previously observed[10] in the stress-strain responses of the 4% and 11% prestrained Mo pillars cannot be explained simply as being due to different initial total dislocation densities. Other possibilities, including increased surface roughness at higher prestrains, which could lead to enhanced surface nucleation of dislocations,[28] need to be investigated in future studies. Similarly, we need to measure dislocation densities over a wider range of pillar sizes than what was investigated here (~500–800 nm), to better understand the transition from stochastic to bulk-like flow behavior as the pillar size increases.[10]

While the total dislocation densities do not appear to be different in the 5% and 11% prestrained pillars, the depth-integrated Laue patterns show increased streaking and broadening of both the Mo and NiAl reflections with increasing prestrain, as shown in Figs. 2(c)–2(e). According to previous analysis of streaked Laue patterns,[24] this is evidence of prestrain-induced geometrically necessary dislocations (GNDs) and/or deviatoric strain gradients in both phases of the composite material. Additional investigations are needed to understand how such increases in GND density and deviatoric strain gradients affect the stress-strain behavior of prestrained pillars.

Finally, the depth dependent dislocation densities plotted in Fig. 7 suggest a higher density in the embedded fibers compared to the exposed pillars. Although the uncertainty of the data preclude any definitive conclusions at this stage, the apparent dislocation density gradient in the exposed pillars (from top to bottom) suggests possible dislocation escape at pillar-free surfaces.

IV. CONCLUSIONS

Elastic strain gradients and dislocation densities in the constituent phases of a NiAl-Mo eutectic composite were studied with polychromatic x-ray microdiffraction as a function of uniaxially applied prestrains of 5% and 11%. In contrast to the as grown NiAl-Mo composite, where along the growth [001] direction the Mo fibers are in compression and the NiAl matrix is in tension (due to the thermal expansion mismatch during solidification), in the 5% and 11% prestrained specimens, the Mo fibers are in tension (0.16% strain) and the NiAl matrix is in slight compression (0.068% strain). This can be explained by considering the mismatch in yield strains for Mo and NiAl and the elastic constraints imposed during unloading after prestraining. When the NiAl matrix is etched back to expose Mo pillars, the tops of the pillars (both for 5% and 11% prestrain) are almost completely relaxed. Their lattice parameter is nearly the same as that of the pillars produced from the as-grown eutectic. The dislocation density in the Mo pillars after prestraining (both for 5% and 11% prestrains) is at least two orders of magnitude higher than that in the as-grown pillars and reaches a value of $\sim 10^9$ cm^{-2}. This explains why the prestrained pillars are significantly weaker than the as-grown ones. Within experimental uncertainty, no difference could be discerned between the total dislocation densities in the Mo phase after 5% and 11% prestrain. In contrast, in the NiAl matrix, the dislocation density increases with increasing prestrain. The amount of streaking in the Laue spots increases with increasing prestrain, indicating that although the total dislocation densities in the 5% and 11% prestrained Mo pillars are not significantly different, the GND density increases with increasing prestrain in both Mo and NiAl. Additional characterization of the prestrained pillars is needed to explain the dramatically different stress-strain behavior of the 4% and 11% prestrained pillars observed in Ref. 10.

ACKNOWLEDGMENTS

This research was sponsored by the Division of Materials Sciences and Engineering, Office of Basic Energy Sciences, U.S. Department of Energy. Data collection with PXM was carried out on beamline ID-34-E at the Advanced Photon Source, Argonne, IL, which is supported by the Office of Basic Energy Sciences, U.S. Department of Energy, under contract No. W-31-109-ENG-38. The authors thank the anonymous reviewers for suggesting several useful changes which have significantly improved the clarity of the manuscript.

REFERENCES

1. M.D. Uchic, D.M. Dimiduk, J.N. Florando, and W.D. Nix: Exploring specimen size effects in plastic deformation of Ni_3(Al, Ta), in *Defect Properties and Related Phenomena in Intermetallic Alloys*, edited by E.P. George, H. Inui, M.J. Mills, and G. Eggeler (Mater. Res. Soc. Symp. Proc. **753,** Warrendale, PA, 2003), p. 27.
2. M.D. Uchic, D.M. Dimiduk, J.N. Florando, and W.D. Nix: Sample dimensions influence strength and crystal plasticity. *Science* **305,** 986 (2004).
3. D.M. Dimiduk, M.D. Uchic, and T.A. Parthasarathy: Size-affected single-slip behavior of pure nickel microcrystals. *Acta Mater.* **53,** 4065 (2005).
4. J.R. Greer and W.D. Nix: Nanoscale gold pillars strengthened through dislocation starvation. *Phys. Rev. B* **73,** 255410 (2006).
5. C.A. Volkert and E.T. Lilleodden: Size effects in the deformation of sub-micron Au columns. *Philos. Mag.* **86,** 5567 (2006).
6. D. Kiener, C. Motz, T. Schoberl, M. Jenko, and G. Dehm: Determination of mechanical properties of copper at the micron scale. *Adv. Eng. Mater.* **8,** 1119 (2006).
7. Z.W. Shan, R.K. Mishra, S.A. Syed Asif, O.L. Warren, and A.M. Minor: Mechanical annealing and source-limited deformation in submicrometre-diameter Ni crystals. *Nat. Mater.* **7,** 115 (2007).
8. H. Bei and E.P. George: Microstructures and mechanical properties of a directionally solidified NiAl-Mo eutectic alloy. *Acta Mater.* **53,** 69 (2005).
9. H. Bei, S. Shim, E.P. George, M.K. Miller, E.G. Herbert, and G.M. Pharr: Compressive strengths of molybdenum alloy micropillars prepared using a new technique. *Scr. Mater.* **57,** 397 (2007).

10. H. Bei, S. Shim, G.M. Pharr, and E.P. George: Effects of prestrain on the compressive stress-strain response of Mo-alloy single-crystal micropillars. *Acta Mater.* **56,** 4762 (2008).
11. H. Bei, Y.F. Gao, S. Shim, E.P. George, and G.M. Pharr: Strength differences arising from homogeneous versus heterogeneous dislocation nucleation. *Phys. Rev. B* **77,** 060103(R) (2008).
12. S. Brickmann, J-Y. Kim, and J.R. Greer: Fundamental differences in mechanical behavior between two types of crystals at the nanoscale. *Phys. Rev. Lett.* **100,** 155502 (2008).
13. S. Shim, H. Bei, M.K. Miller, G.M. Pharr, and E.P. George: Effects of focused-ion-beam milling on the compressive behavior of directionally solidified micropillars and the nanoindentation response of an electropolished surface. *Acta Mater.* **57,** 503 (2009).
14. K. Thompson, D. Lawrence, D.J. Larson, J.D. Olson, T.F. Kelly, and B. Gorman: In situ site-specific specimen preparation for atom probe tomography. *Ultramicroscopy* **107,** 131 (2007).
15. J. Mayer, L.A. Giannuzzi, T. Kamino, and J. Michael: TEM sample preparation and FIB-induced damage. *MRS Bull.* **32,** 400 (2007).
16. D. Kiener, C. Motz, M. Rester, M. Jenko, and G. Dehm: Ga+ ion beam damage during focused ion beam preparation of Cu samples. *Mater. Sci. Eng., A* **459,** 262 (2007).
17. D.M. Norfleet, D.M. Dimiduk, S.J. Polasik, M.D. Uchic, and M.J. Mills: Dislocation structures and their relationship to strength in deformed nickel microcrystals. *Acta Mater.* **56,** 2988 (2008).
18. R. Maass, D. Grolimund, S. Van Petegem, M. Willimann, M. Jensen, and H. Van Swygenhoven: Defect structure in micropillars using x-ray microdiffraction. *Appl. Phys. Lett.* **89,** 151905 (2006).
19. R. Maass, S. Van Petegem, H. Van Swygenhoven, P.M. Derlet, C.A. Volkert, and D. Grolimund: Time-resolved Laue diffraction of deforming micropillars. *Phys. Rev. Lett.* **99,** 145505 (2007).
20. H. Bei, R.I. Barabash, G.E. Ice, W. Liu, J. Tischler, and E.P. George: Spatially resolved strain measurements in Mo-alloy micropillars by differential aperture x-ray microscopy. *Appl. Phys. Lett.* **93,** 071904 (2008).
21. B.C. Larson, W. Yang, G.E. Ice, J.D. Budai, and J.Z. Tischler: Three-dimensional x-ray structural microscopy with submicron resolution. *Nature* **415,** 887 (2002).
22. H. Bei, E.P. George, D.W. Brown, G.M. Pharr, H. Choo, W.D. Porter, and M.A.M. Bourke: Thermal-expansion behavior of a directionally solidified NiAl-Mo composite investigated by neutron diffraction and dilatometry. *J. Appl. Phys.* **97,** 123503 (2005).
23. A. Misra, Z.L. Wu, M.T. Kush, and R. Gibala: Deformation and fracture behavior of directionally solidified NiAl-Mo and NiAl-Mo(Re) eutectic composites. *Philos. Mag.* **78,** 533 (1998).
24. G.E. Ice and R.I. Barabash: White beam microdiffraction and dislocations gradients, in *Dislocations in Solids*, Vol. 13 (2007), p. 500.
25. R.I. Barabash, G.E. Ice, W. Liu, and O.M. Barabash: Polychromatic microdiffraction characterization of defect gradients in severely-deformed materials. *Micron* **40,** 28 (2009).
26. R.I. Barabash, Y. Gao, Y. Sun, S.Y. Lee, H. Choo, P. Liaw, D. Brown, and G. Ice: Neutron and x-ray diffraction studies and cohesive interface model of the fatigue crack deformation behavior. *Philos. Mag. Lett.* **88,** 553 (2008).
27. D.B. Miracle and R. Darolia: NiAl and its alloys, in *Intermetallic Compounds: Principles and Practice*, Vol. 2, edited by J.H. Westbrook and R.L. Fleischer (John Wiley & Sons, New York, 1995), pp. 53–72.
28. S. Lee, S.M. Han, and W.D. Nix: Uniaxial compression of fcc Au nanopillars on an MgO substrate: The effects of prestraining and annealing. *Acta Mater.* **57,** 4404 (2009).